**Supporting information**

# Theoretical study of *p*-block metal-nitrogen-carbon single-atom catalysts for heterogeneous Fenton-like reaction

Chen Zhou,[a] Haobin Tan,[a] Shengbo Wang,[a] Qiang Liu,[b] Zhenhui Xu,[b] Peng Zhang,[a,*]

Chun Hu[a,*]

[a] Key Laboratory for Water Quality and Conservation of the Pearl River Delta, Ministry of Education, Institute of Environmental Research at Greater Bay, Guangzhou University, Guangzhou 510006, China

[b] *Houma Special Industry Factory, Houma 043000, China*

*Corresponding author

*E-mail: pengzhang85@foxmail.com huchun@gzhu.edu.cn

**Computational methods**

All spin-polarized calculations were performed using DMol[3] code based on density function theory (DFT).[1,2] The generalized gradient approximation (GGA) with PW91 was adopted as the exchange and correlation function. All electron relativistic core treatment was used by considering the relativistic effect of core electrons. The double numerical plus polarization (DNP) basis set was implemented to describe atomic orbitals.[3] The smearing value was set at 0.005 Ha to accelerate the energy convergence speed. The Brillouin zone was sampled using the 1 × 1 × 1 and 9 × 9 × 1 Monkhorst-Pack k-points grids for structure relaxations and electronic structure computations, respectively. The convergence test for k-point mesh was performed. As shown in Table S7, the adsorption energies of OH* on $InC_4$ were similar as the k-point mesh varying from 1×1×1 to 4×4×1. In the geometry structural optimization, the convergence tolerances of energy, maximum force, and displacement are $1.0 \times 10^{-5}$ Ha, 0.002 Ha/Å, and 0.005 Å, respectively[4] The activation energies for the elemental step were determined by the LST/QST method.[5] Previous work has confirmed that the water solvent changes the energies of O-containing species and then barrier energies.[6] In this work, a conductor-like screening model (COSMO) was used to describe the water solvent environment, and the dielectric constant was set as 78.54 for the $H_2O$ solvent.[7] In order to describe the van der Waals interaction, the DFT-D method within OBS scheme was employed.[8]

In this work, nine p-block metal (Al, Ga, In, Tl, Ge, Sn, Pd, Sb, and Bi) -$N_4$, -$N_2C_2$, -$C_4$ moiety embedded graphene nanosheets (double carbon vacancies) were

investigated as SACs. A 5 × 5 supercell slab of the graphene single layer was built as the substrate model.[9,10] The length of the c-axis was set as 20 Å for a vacuum layer to avoid the interaction between two periodic units. The optimized lattice constants were shown in Table S8. The adsorption energy ($E_{ads}$) was calculated as $E_{ads} = E_{sys} - E_{cat} - E_{mol}$, where $E_{sys}$, $E_{cat}$, and $E_{mol}$ represent the total energies of the adsorption system, the catalyst, and the adsorbate molecule, respectively.

In order to evaluate the bonding strength between the PM atom and the substrate, the binding energies $E_b$ were calculated as: $E_b = E_{PM/N/C} - E_{N/C} - E_{PM}$, where $E_{N/C}$and $E_{PM}$ were the energies of N/C doped graphene nanosheet (double carbon vacancies) and one isolated PM atom calculated by DFT, respectively. Furthermore, the cohesive energies in bulk metal ($E_{coh}$) were calculated as: $E_{coh} = \mu_{PM(bulk)} - E_{PM}$ where $\mu_{PM(bluk)}$ was the calculated chemical potential of PM atom from the most stable bulk by DFT. The *p*-band center is defined as $\varepsilon_p = \frac{\int_{-\infty}^{+\infty} E \times \rho_p dE}{\int_{-\infty}^{+\infty} \rho_p dE}$, where $\rho_p$ is the density of *p*-band of *p*-block main-group metals.[11]

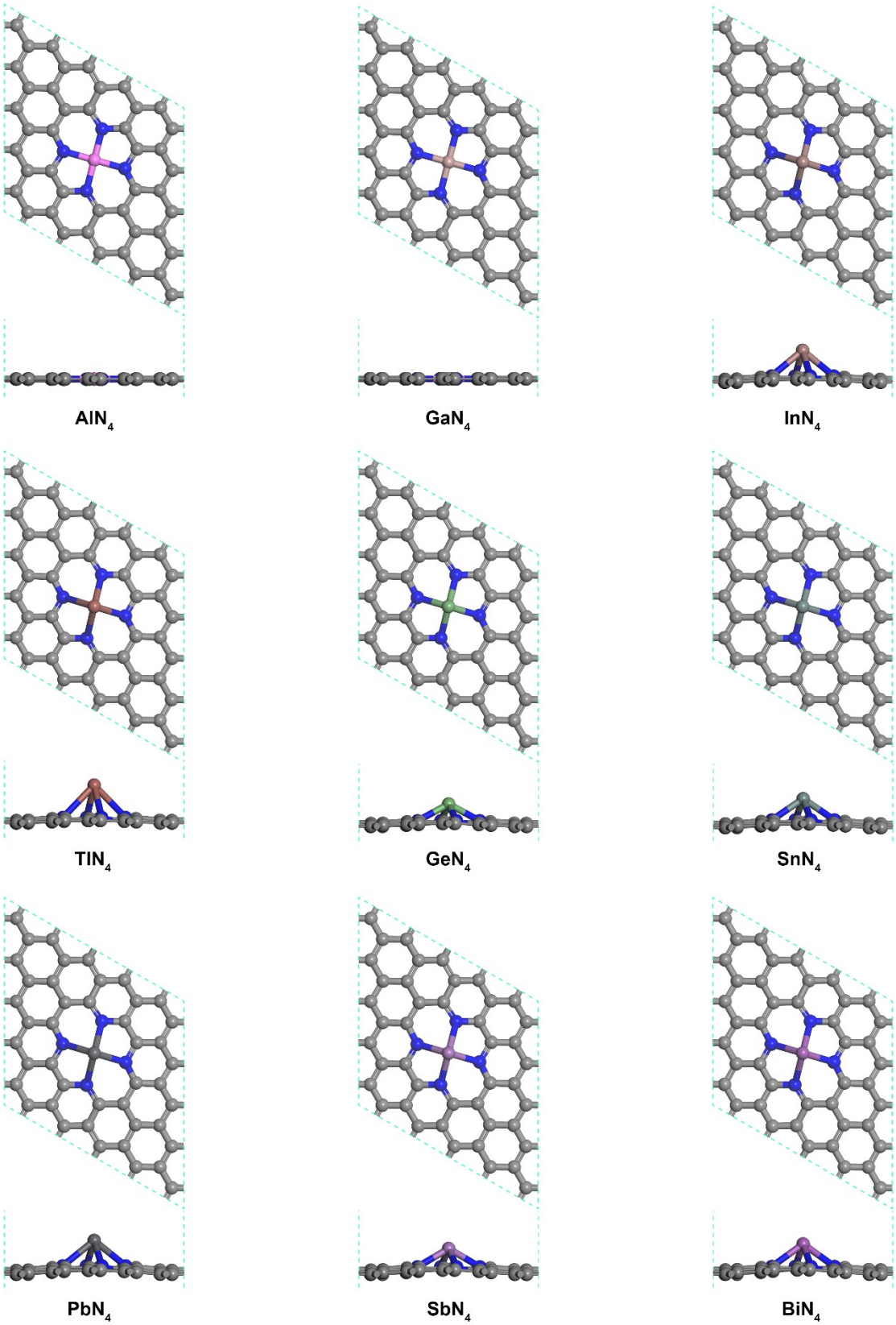


Fig. S1 Optimized geometric configurations of PM-$N_4$ embedded graphene, containing top view and side view (Grey, blue spheres represent C, N atoms, respectively).

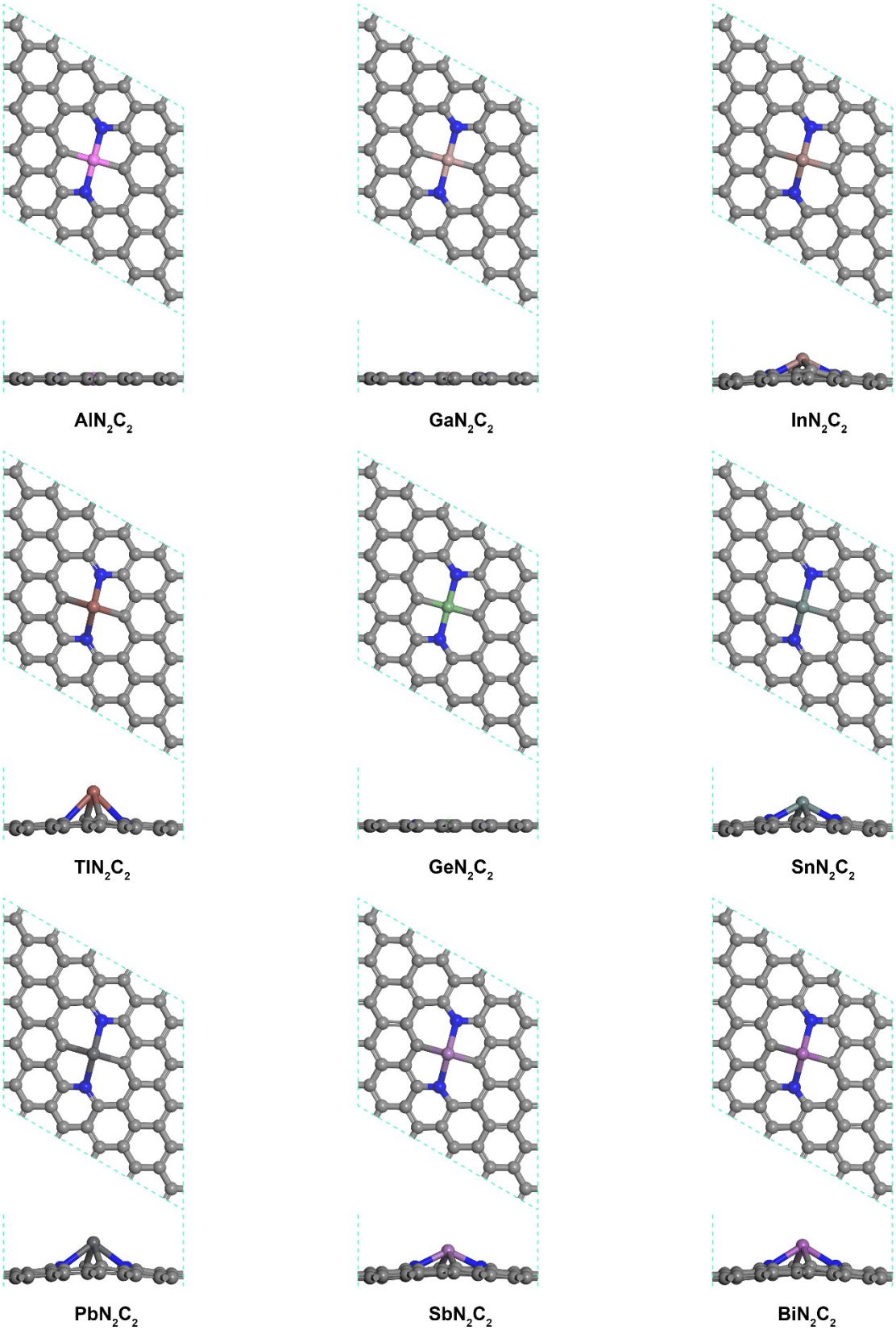


Fig. S2 Optimized geometric configurations of PM-$N_2C_2$ embedded graphene, containing top view and side view (Grey, blue spheres represent C, N atoms, respectively).

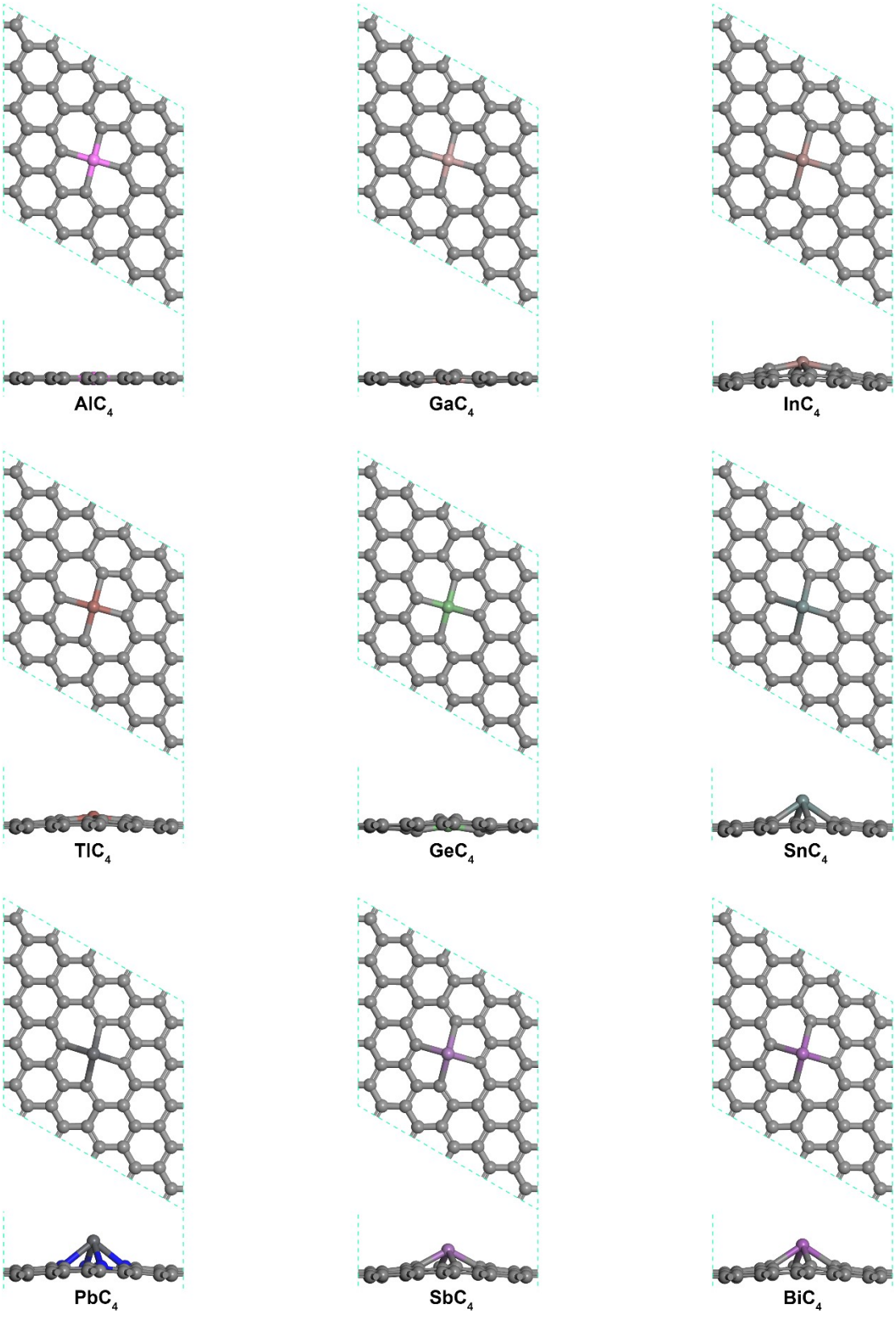


Fig. S3 Optimized geometric configurations of PM-$C_4$ embedded graphene, containing top view and side view (Grey, blue spheres represent C, N atoms, respectively).

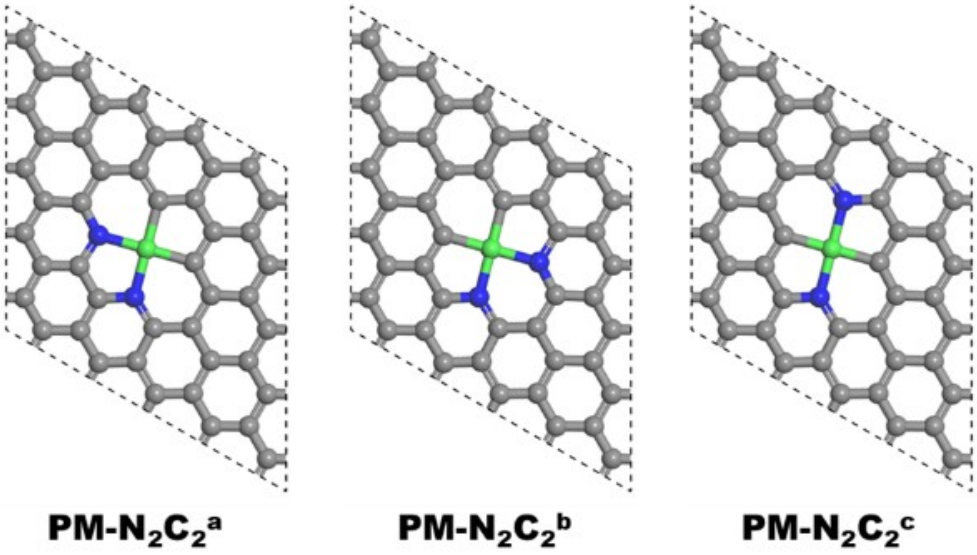


Fig. S4 Schematic illustrations of PM-$N_2C_2^a$, PM-$N_2C_2^b$ and PM-$N_2C_2^c$ three allotropic structures of PM-$N_2C_2$.

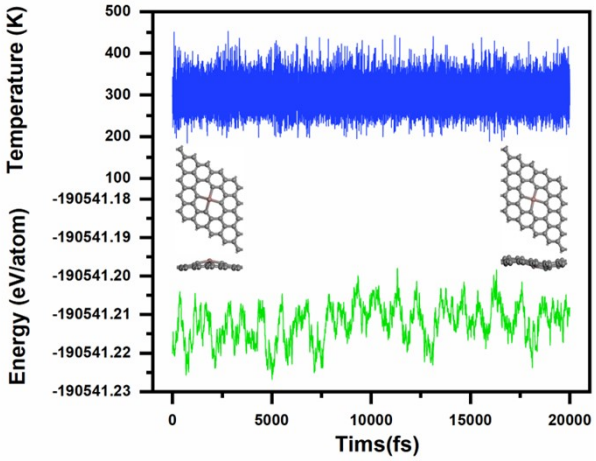


Fig. S5 Evolution of the total energy per atom and the temperature within 10000 fs AIMD simulation at 300 K for $InC_4$. The inset diagrams show the atomic structure at start and end of the AIMD simulation.

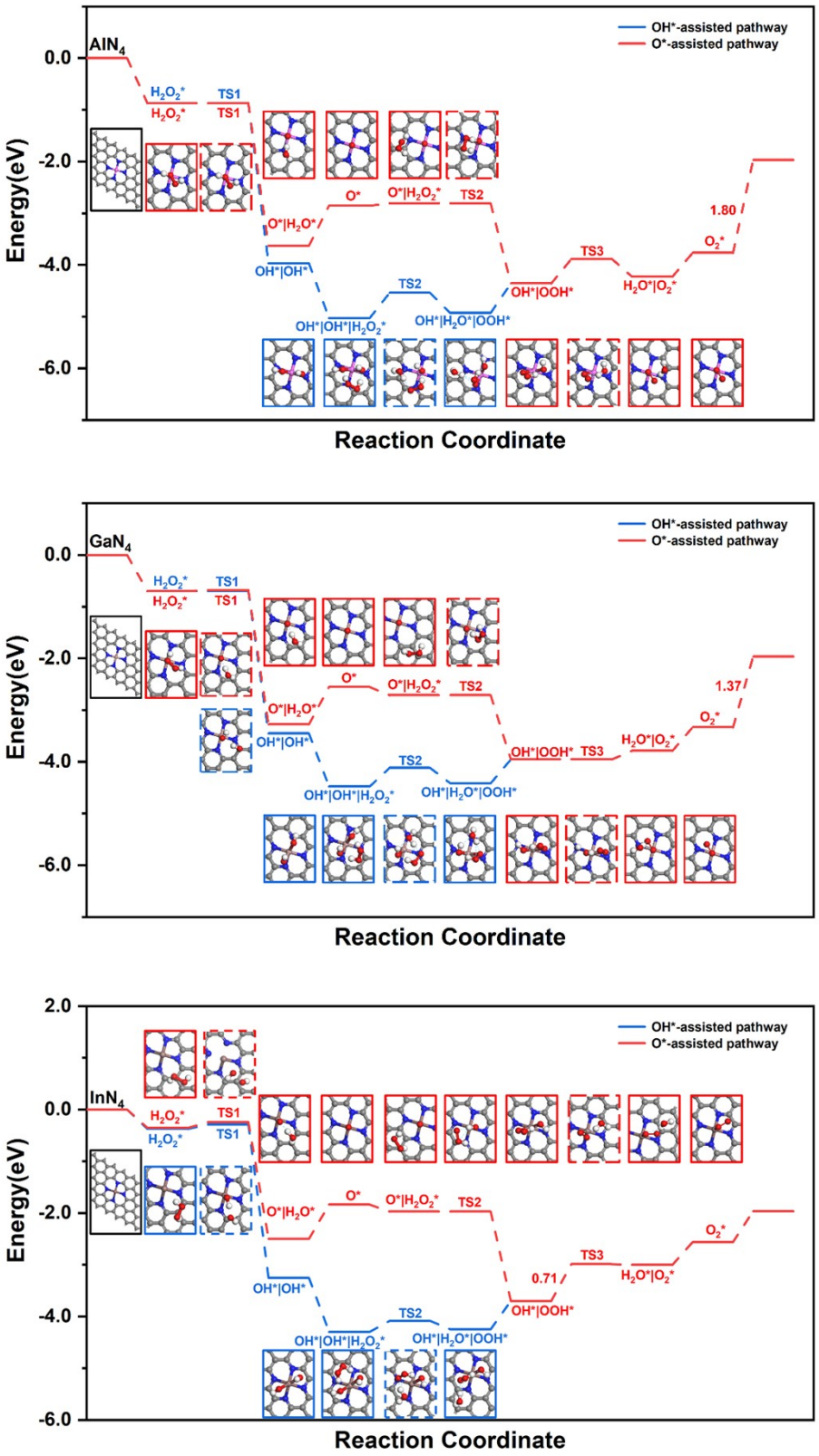


Fig. S6 The reaction energy diagram of $H_2O_2$ decomposition on the $AlN_4$, $GaN_4$, $InN_4$.

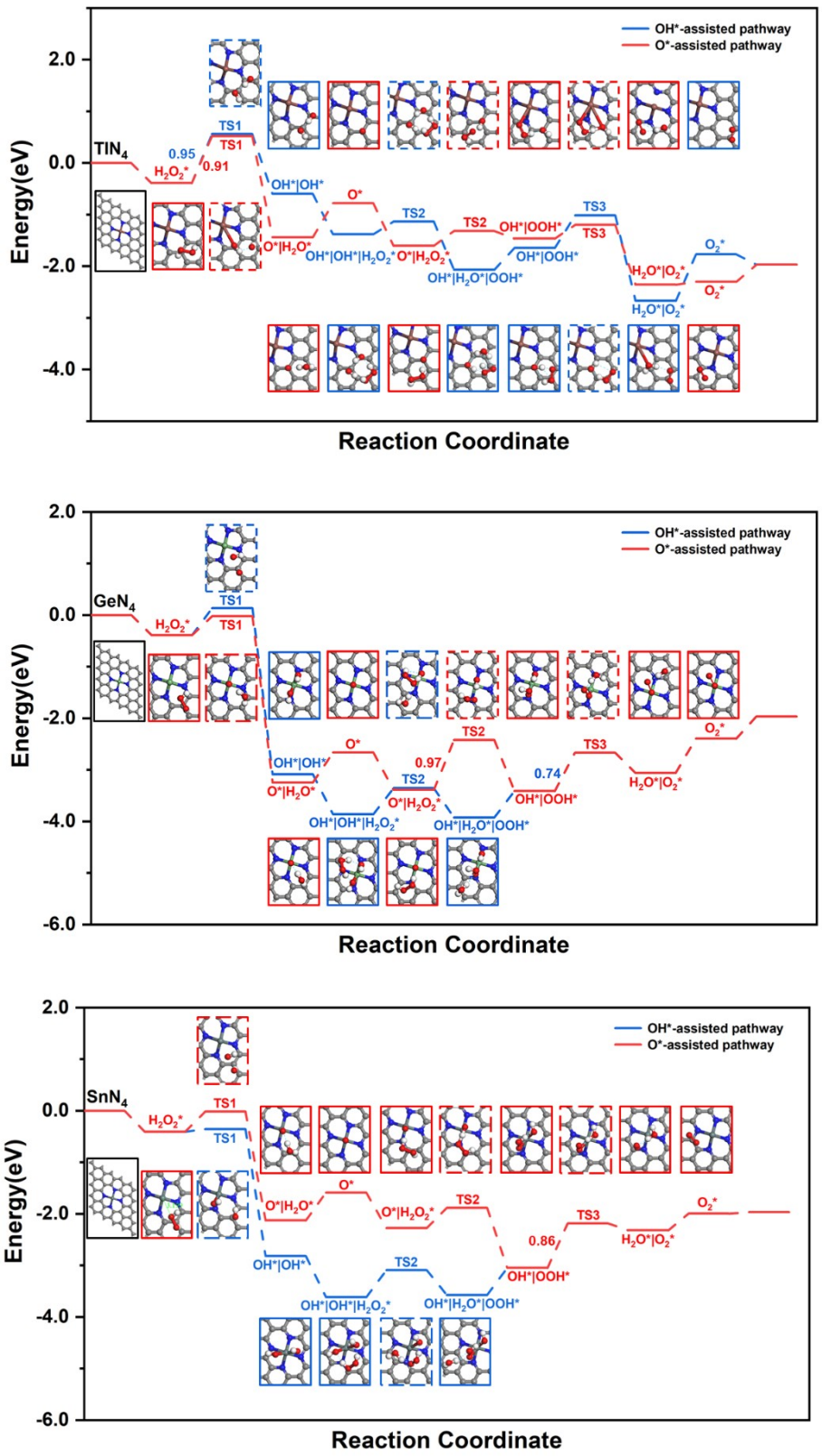


Fig. S7 The reaction energy diagram of $H_2O_2$ decomposition on the $TlN_4$, $GeN_4$, $SnN_4$.

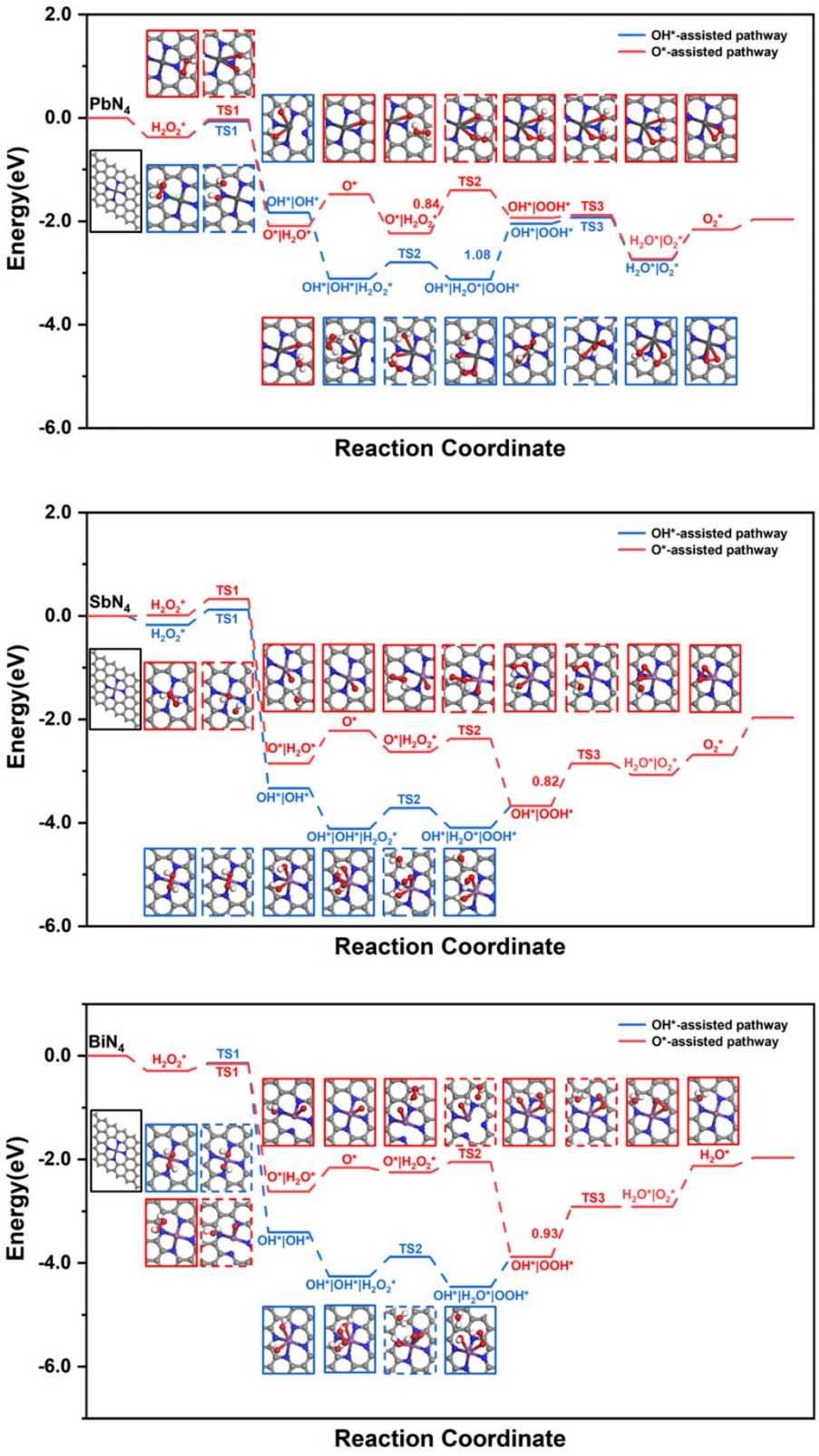


Fig. S8 The reaction energy diagram of $H_2O_2$ decomposition on the $PbN_4$, $SbN_4$, $BiN_4$.

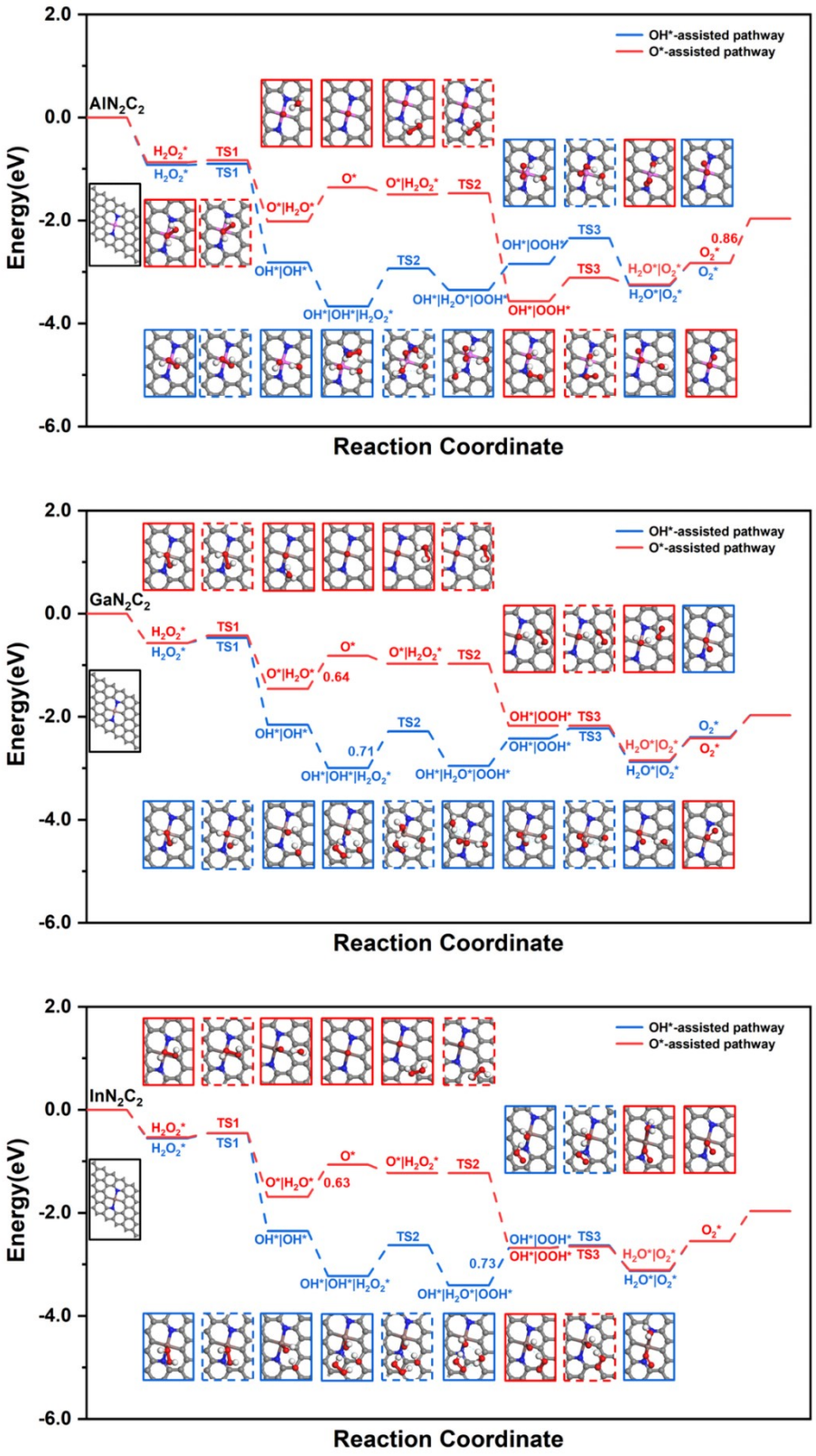


Fig. S9 The reaction energy diagram of $H_2O_2$ decomposition on the $AlN_2C_2$, $GaN_2C_2$, $InN_2C_2$.

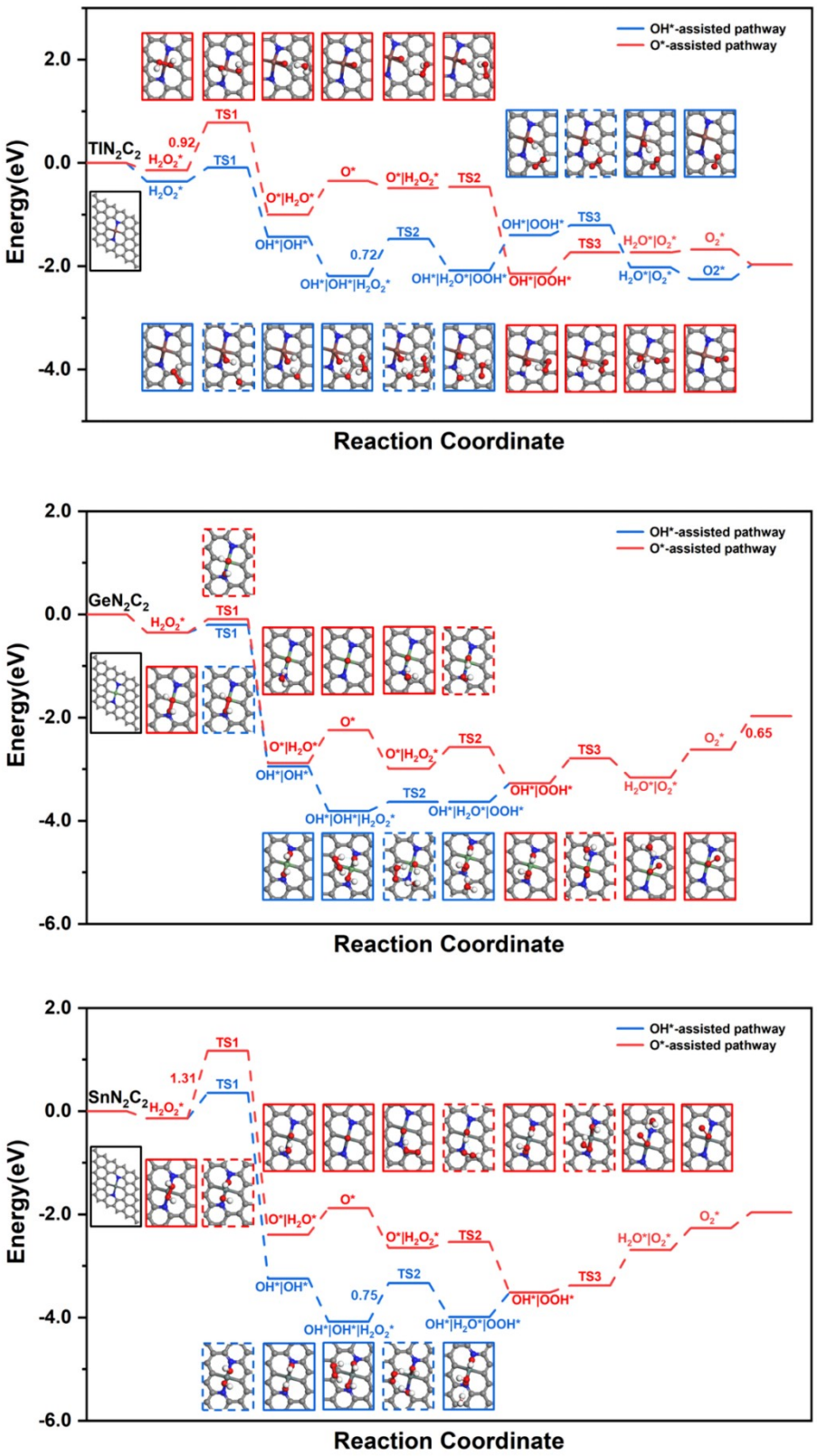


Fig. S10 The reaction energy diagram of $H_2O_2$ decomposition on the $TlN_2C_2$, $GeN_2C_2$, $SnN_2C_2$.

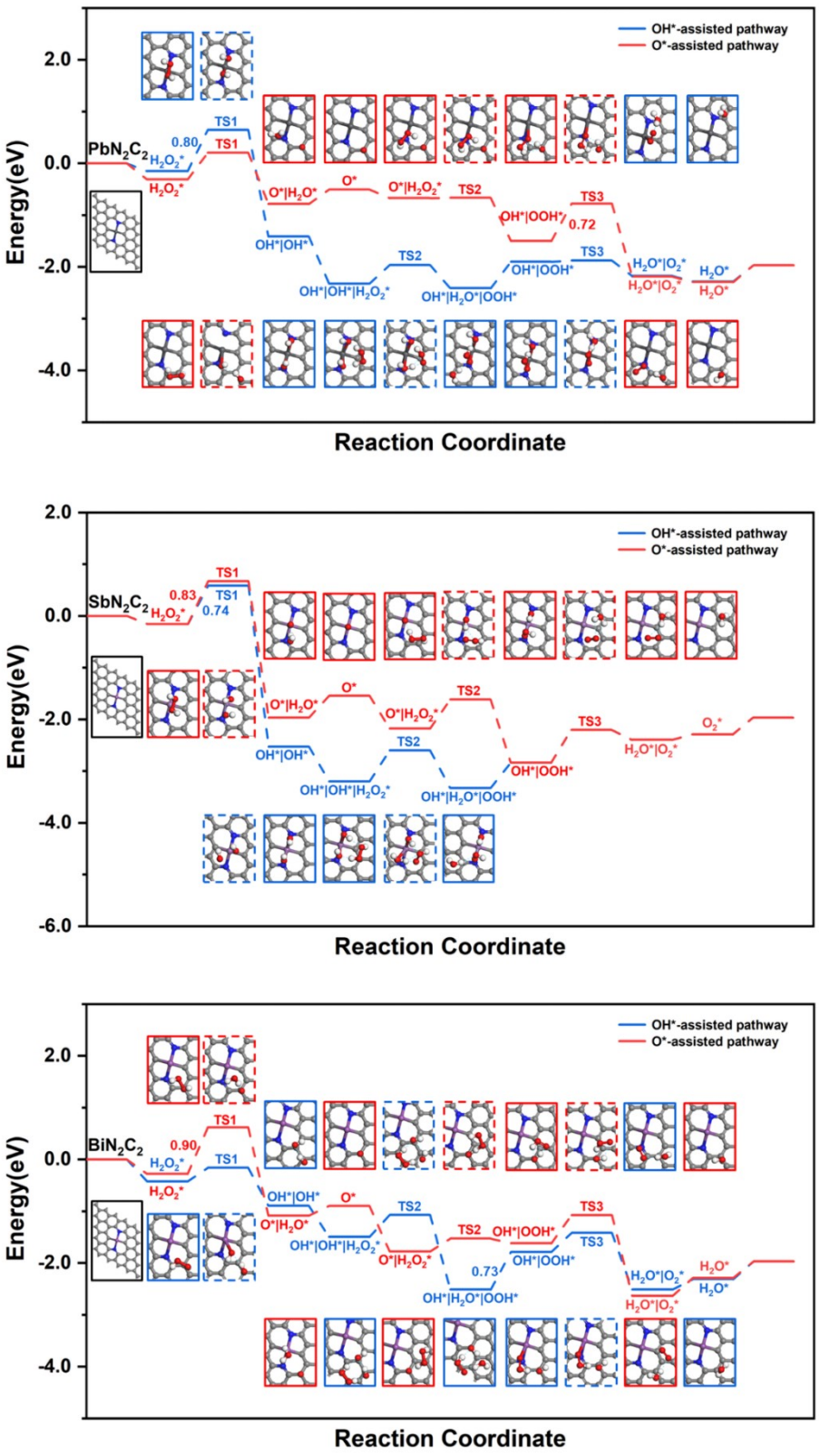


Fig. S11 The reaction energy diagram of $H_2O_2$ decomposition on the $PbN_2C_2$, $SbN_2C_2$, $BiN_2C_2$.

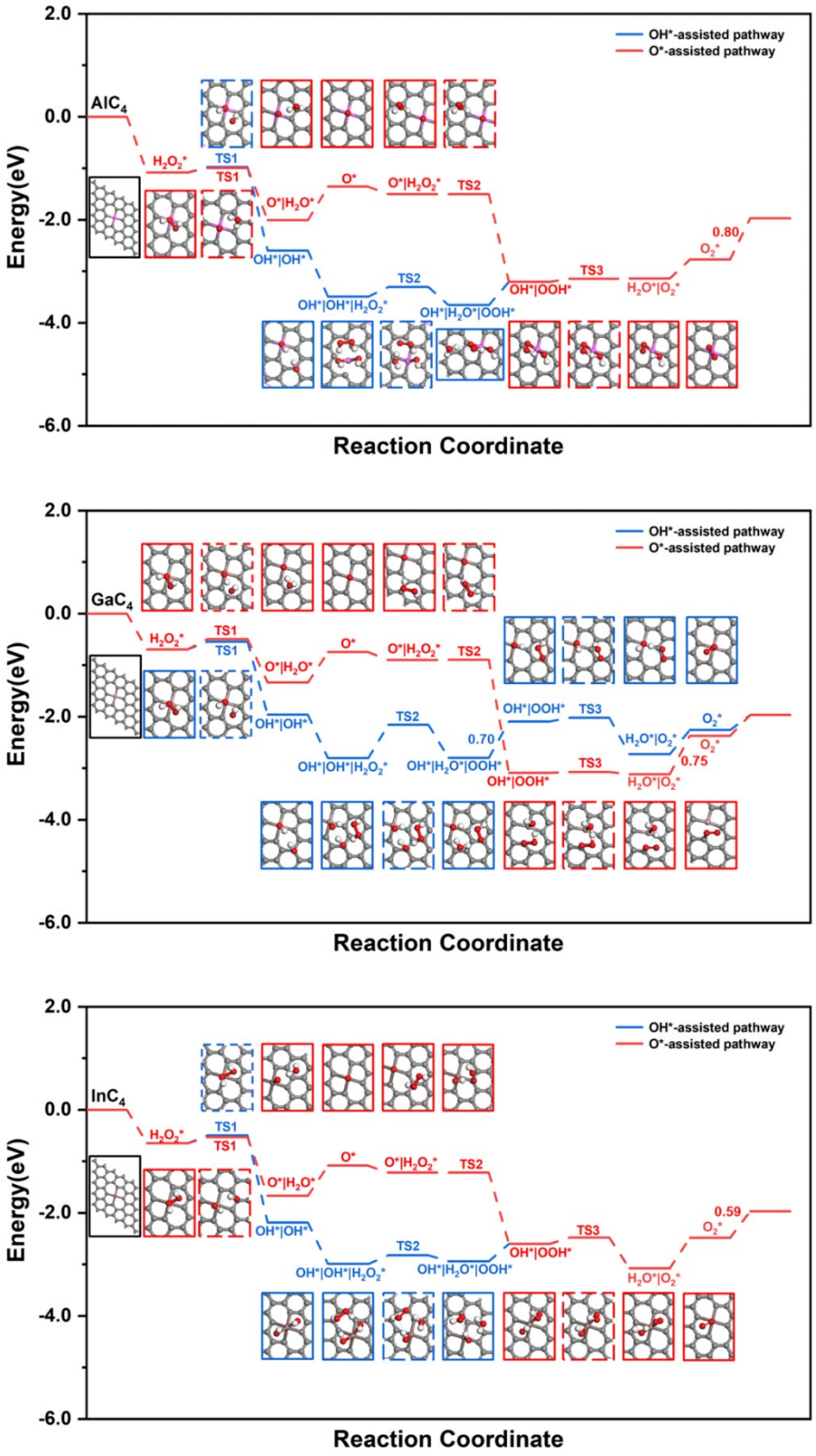


Fig. S12 The reaction energy diagram of $H_2O_2$ decomposition on the $AlC_4$, $GaC_4$, $InC_4$.

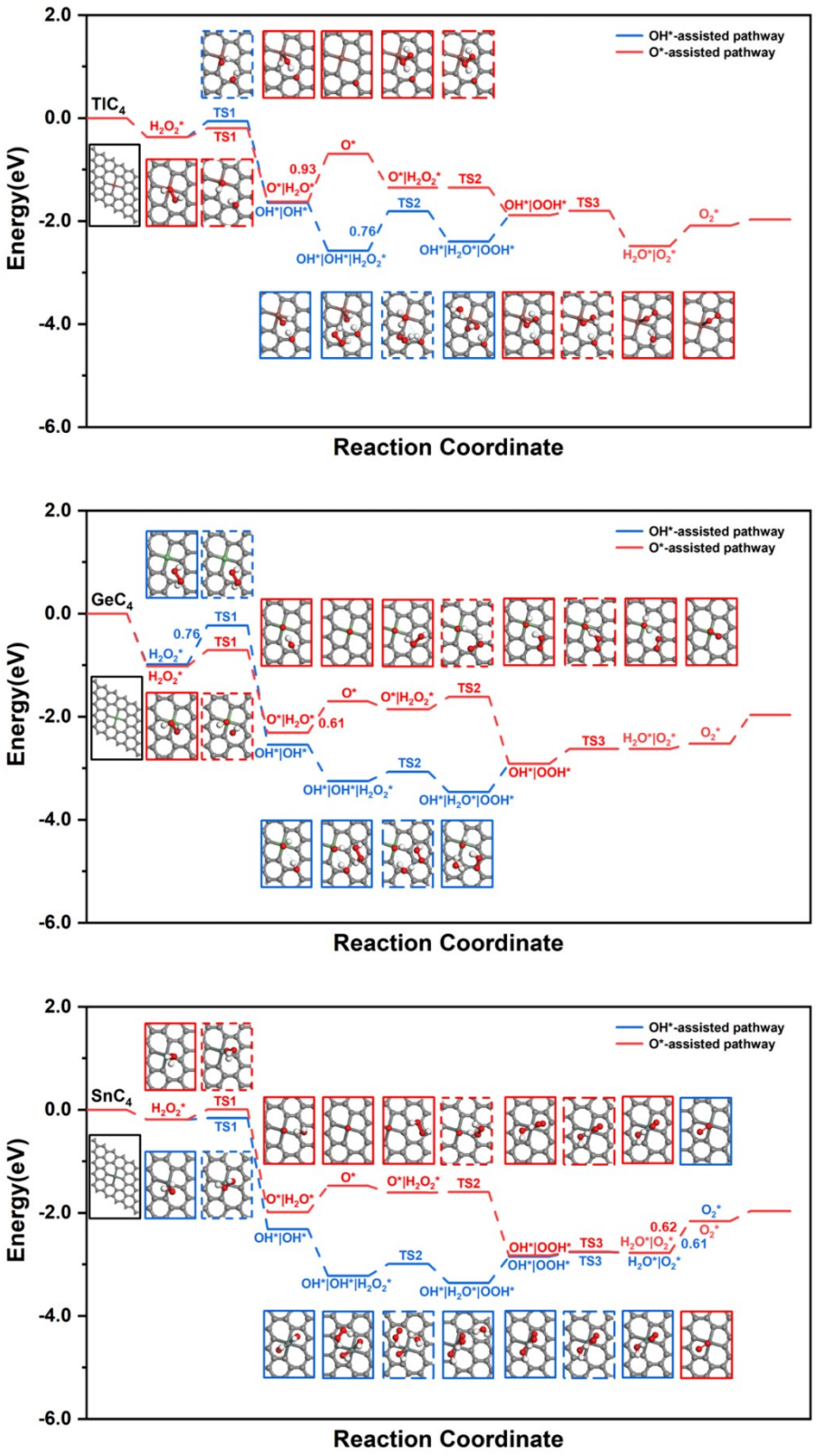


Fig. S13 The reaction energy diagram of $H_2O_2$ decomposition on the $TlC_4$, $GeC_4$, $SnC_4$.

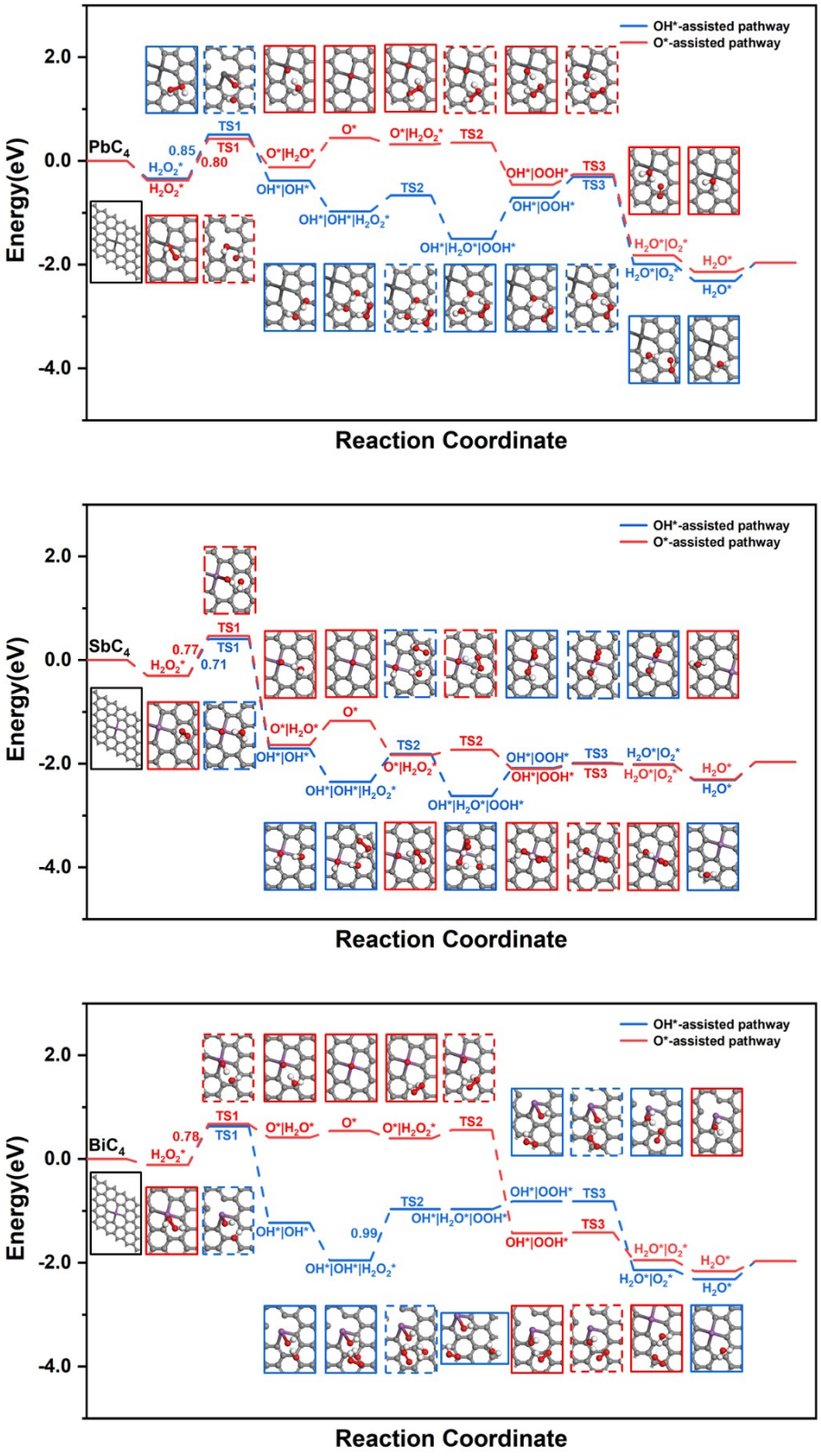


Fig. S14 The reaction energy diagram of $H_2O_2$ decomposition on the $PbC_4$, $SbC_4$, $BiC_4$.

Table S1. The energy (eV) of PM-$N_2C_2$[a], PM-$N_2C_2$[b] and PM-$N_2C_2$[c]. All results were in unit of eV and the energy of PM-$N_2C_2$[c] was set as 0 eV.

| PM-$N_2C_2$ | PM-$N_2C_2$[a] | PM-$N_2C_2$[b] | PM-$N_2C_2$[c] |
|---|---|---|---|
| $AlN_2C_2$ | 0.32 | 0.35 | 0 |
| $GaN_2C_2$ | 0.51 | 0.50 | 0 |
| $InN_2C_2$ | 0.53 | 0.56 | 0 |
| $TlN_2C_2$ | 0.06 | -0.92 | 0 |
| $GeN_2C_2$ | 0.53 | 0.59 | 0 |
| $SnN_2C_2$ | 0.35 | 0.16 | 0 |
| $PbN_2C_2$ | 0.05 | -0.12 | 0 |
| $SbN_2C_2$ | 0.06 | 0.17 | 0 |
| $BiN_2C_2$ | 0.00 | -0.10 | 0 |

Table S2. The Mulliken charge ($C_M$), the Hershfield charge ($C_H$), the highest occupied molecular orbital (HOMO) and the *p*-band centre ($\varepsilon_p$) of the *p*-block metal atoms in PM-SACs.

| PM moiety | $C_M$(e) | $C_H$(e) | HOMO(eV) | $\varepsilon_p$(eV) |
|---|---|---|---|---|
| $AlN_4$ | 1.09 | 0.52 | -0.18 | -2.35 |
| $GaN_4$ | 1.05 | 0.53 | -0.18 | -2.00 |
| $InN_4$ | 0.58 | 0.26 | -0.21 | -0.94 |
| $TlN_4$ | 0.72 | 0.45 | -0.21 | 2.04 |
| $GeN_4$ | 0.52 | 0.32 | -0.17 | -1.61 |
| $SnN_4$ | 0.84 | 0.45 | -0.17 | -0.09 |
| $PbN_4$ | 1.06 | 0.68 | -0.16 | 0.59 |
| $SbN_4$ | 1.06 | 0.67 | -0.17 | -0.91 |
| $BiN_4$ | 1.25 | 0.83 | -0.17 | -0.82 |
| $AlN_2C_2$ | 0.90 | 0.44 | -0.21 | -1.60 |
| $GaN_2C_2$ | 0.77 | 0.42 | -0.21 | -1.66 |
| $InN_2C_2$ | 1.08 | 0.53 | -0.21 | -2.05 |
| $TlN_2C_2$ | 0.58 | 0.33 | -0.19 | 0.54 |
| $GeN_2C_2$ | 0.66 | 0.35 | -0.19 | -2.37 |
| $SnN_2C_2$ | 0.67 | 0.30 | -0.20 | -2.10 |
| $PbN_2C_2$ | 0.70 | 0.42 | -0.18 | 1.79 |
| $SbN_2C_2$ | 0.74 | 0.46 | -0.21 | -2.29 |
| $BiN_2C_2$ | 0.93 | 0.61 | -0.21 | -1.50 |
| $AlC_4$ | 0.89 | 0.43 | -0.20 | -1.07 |
| $GaC_4$ | 0.68 | 0.38 | -0.19 | -1.73 |
| $InC_4$ | 1.02 | 0.51 | -0.18 | -1.33 |
| $TlC_4$ | 0.66 | 0.50 | -0.21 | -2.39 |
| $GeC_4$ | 0.62 | 0.37 | -0.21 | -2.10 |
| $SnC_4$ | 0.47 | 0.27 | -0.21 | -1.65 |
| $PbC_4$ | 0.63 | 0.43 | -0.21 | -0.11 |
| $SbC_4$ | 0.52 | 0.38 | -0.19 | -2.95 |
| $BiC_4$ | 0.70 | 0.51 | -0.21 | -1.94 |

Table S3. Elementary reactions based on those close-shell species and intermediates for the decomposition of $H_2O_2$.

| No. | Elementary reaction |
|---|---|
| 1 | $H_2O_2 + * \leftrightarrow H_2O_2*$ |
| 2 | $H_2O* \leftrightarrow H_2O + *$ |
| 3 | $O_2* \leftrightarrow O_2 + *$ |
| 4 | $H*+ H* \leftrightarrow H_2 + 2*$ |
| 5 | $H_2O_2* + * \leftrightarrow OH* + OH*$ |
| 6 | $OOH* + * \leftrightarrow O* + OH*$ |
| 7 | $O_2* + * \leftrightarrow O* + O*$ |
| 8 | $OH* + * \leftrightarrow O* + H*$ |
| 9 | $H_2O* + * \leftrightarrow OH* + H*$ |
| 10 | $OOH* + * \leftrightarrow O_2* + H*$ |
| 11 | $H_2O_2* + * \leftrightarrow OOH* + H*$ |
| 12 | $H_2O* + O* \leftrightarrow OH* + OH*$ |
| 13 | $H_2O_2* + O* \leftrightarrow OOH* + OH*$ |
| 14 | $H_2O_2* + OH* \leftrightarrow OOH* + H_2O*$ |
| 15 | $OOH* + O* \leftrightarrow O_2* + OH*$ |
| 16 | $OOH* + OH* \leftrightarrow O_2* + H_2O*$ |
| 17 | $H_2O_2* + O_2* \leftrightarrow OOH* + OOH*$ |

Table S4. The reaction energies and barrier energies of the direct dehydrogenation and the O-O bond scission to form two OH* or O* and $H_2O$*of the first adsorbed $H_2O_2$*.

| | $H_2O_2$*-OOH*+H* | | $H_2O_2$*-OH*+OH* | | $H_2O_2$*-O*+$H_2O$* | |
|---|---|---|---|---|---|---|
| PM moiety | reaction energy(eV) | barrier energy(eV) | reaction energy(eV) | barrier energy(eV) | reaction energy(eV) | barrier energy(eV) |
| $AlN_4$ | 0.08 | 2.01 | -3.10 | 0.00 | -2.76 | 0.00 |
| $GaN_4$ | 0.28 | 2.35 | -2.75 | 0.00 | -2.58 | 0.02 |
| $InN_4$ | 0.95 | 1.11 | -2.88 | 0.08 | -2.15 | 0.11 |
| $TlN_4$ | 1.61 | 1.46 | -0.10 | 0.48 | 0.31 | 0.70 |
| $GeN_4$ | 1.10 | 2.02 | -2.70 | 0.52 | -2.86 | 0.37 |
| $SnN_4$ | 1.78 | 1.97 | -2.41 | 0.05 | -1.72 | 0.39 |
| $PbN_4$ | 1.71 | 1.73 | -1.46 | 0.30 | -1.72 | 0.34 |
| $SbN_4$ | 0.51 | 1.90 | -3.16 | 0.30 | -2.86 | 0.31 |
| $BiN_4$ | 0.70 | 0.92 | -3.12 | 0.15 | -2.14 | 0.14 |
| $AlN_2C_2$ | 0.16 | 0.86 | -0.39 | 0.02 | -1.15 | 0.04 |
| $GaN_2C_2$ | 0.44 | 0.95 | -1.59 | 0.10 | -0.89 | 0.14 |
| $InN_2C_2$ | 0.32 | 2.22 | -1.80 | 0.09 | -1.15 | 0.08 |
| $TlN_2C_2$ | 0.86 | 1.49 | -1.07 | 0.27 | -1.11 | 0.51 |
| $GeN_2C_2$ | -0.07 | 0.95 | -2.59 | 0.15 | -2.53 | 0.26 |
| $SnN_2C_2$ | 2.95 | 3.02 | -3.11 | 0.50 | -2.25 | 1.31 |
| $PbN_2C_2$ | 1.15 | 0.24 | -1.26 | 0.80 | -0.47 | 0.52 |
| $SbN_2C_2$ | 1.73 | 3.30 | -2.37 | 0.74 | -1.81 | 0.83 |
| $BiN_2C_2$ | 0.87 | 2.67 | -1.43 | 0.36 | -0.88 | 0.72 |
| $AlC_4$ | -0.07 | 0.74 | -1.52 | 0.10 | -0.93 | 0.09 |
| $GaC_4$ | 0.25 | 0.78 | -1.27 | 0.15 | -0.44 | 0.20 |
| $InC_4$ | 0.21 | 0.91 | -1.54 | 0.15 | -1.02 | 0.12 |
| $TlC_4$ | 0.69 | 1.04 | -1.28 | 0.31 | -1.26 | 0.17 |
| $GeC_4$ | 1.24 | 1.17 | -1.56 | 0.03 | -1.29 | 0.31 |
| $SnC_4$ | 1.12 | 2.02 | -2.13 | 0.03 | -1.80 | 0.19 |
| $PbC_4$ | 2.22 | 1.71 | -0.04 | 0.85 | 0.26 | 0.22 |
| $SbC_4$ | 1.90 | 2.47 | -1.40 | 0.71 | -1.33 | 0.77 |
| $BiC_4$ | 1.78 | 2.20 | -1.12 | 0.69 | 0.16 | 0.62 |

Table S5. The reaction energies and barrier energies of second $H_2O_2$* directly decompose to from $H_2O$* and O*, and H-transfer with O* to from OH* and OOH*.

| | O*+$H_2O_2$*-O*+O*+$H_2O$* | | O*+$H_2O_2$*-OH*+OOH* | |
|---|---|---|---|---|
| PM moiety | reaction energy(eV) | barrier energy(eV) | reaction energy(eV) | barrier energy(eV) |
| $AlN_4$ | -0.55 | 1.48 | -1.55 | 0.00 |
| $GaN_4$ | -0.93 | 1.30 | -1.24 | 0.00 |
| $InN_4$ | -0.71 | 1.59 | -1.73 | 0.00 |
| $TlN_4$ | -0.11 | 1.25 | -0.72 | 0.03 |
| $GeN_4$ | -0.44 | 0.92 | -0.02 | 0.97 |
| $SnN_4$ | -0.60 | 1.57 | -0.77 | 0.39 |
| $PbN_4$ | -0.73 | 1.27 | -1.40 | 0.03 |
| $SbN_4$ | -1.25 | 0.45 | -1.04 | 0.26 |
| $BiN_4$ | -0.49 | 0.86 | -1.04 | 0.20 |
| $AlN_2C_2$ | -0.27 | 1.64 | -1.80 | 0.02 |
| $GaN_2C_2$ | -0.85 | 1.64 | -1.20 | 0.00 |
| $InN_2C_2$ | -0.52 | 2.17 | -1.45 | 0.01 |
| $TlN_2C_2$ | -0.12 | 1.35 | -1.66 | 0.02 |
| $GeN_2C_2$ | 1.61 | 2.56 | -0.28 | 0.42 |
| $SnN_2C_2$ | -0.72 | 0.56 | -0.86 | 0.12 |
| $PbN_2C_2$ | -1.08 | 1.45 | -0.83 | 0.01 |
| $SbN_2C_2$ | -0.63 | 0.88 | -0.66 | 0.56 |
| $BiN_2C_2$ | -0.80 | 1.61 | -1.90 | 0.00 |
| $AlC_4$ | -0.33 | 1.86 | -1.72 | 0.00 |
| $GaC_4$ | -0.88 | 1.95 | -2.19 | 0.00 |
| $InC_4$ | -0.45 | 1.80 | -1.38 | 0.00 |
| $TlC_4$ | 1.81 | 1.50 | -1.67 | 0.03 |
| $GeC_4$ | -0.85 | 1.95 | 0.00 | 0.00 |
| $SnC_4$ | -0.96 | 1.47 | -1.22 | 0.01 |
| $PbC_4$ | -0.73 | 1.65 | -0.78 | 0.03 |
| $SbC_4$ | -0.71 | 1.39 | -0.27 | 0.10 |
| $BiC_4$ | -0.96 | 1.41 | -1.83 | 0.16 |

Table S6. The adsorption energies of O* and OH* on the PM/N/C SACs, the integrated COOP (ICOOP) of OH* adsorbed on the *p*-block metal atoms in PM/N/C SACs and the activation energies of rate-determining step ($E_{RDS}$) involved in the $H_2O_2$ decomposition on PM/N/C SACs.

| PM moiety | $E_{ads}$-O(eV) | $E_{ads}$-OH(eV) | ICOOP-OH | $E_{RDS}$(eV) |
|---|---|---|---|---|
| $AlN_4$ | -1.87 | -4.78 | 0.19 | 1.80 |
| $GaN_4$ | -1.57 | -4.23 | 0.17 | 1.37 |
| $InN_4$ | -0.85 | -3.34 | 0.14 | 0.71 |
| $TlN_4$ | 1.49 | -1.27 | 0.06 | 0.91 |
| $GeN_4$ | -1.68 | -3.04 | 0.16 | 0.74 |
| $SnN_4$ | -0.60 | -1.91 | 0.11 | 0.86 |
| $PbN_4$ | 0.47 | -2.45 | 0.07 | 0.84 |
| $SbN_4$ | -1.24 | -3.15 | 0.09 | 0.82 |
| $BiN_4$ | -1.18 | -3.15 | 0.08 | 0.93 |
| $AlN_2C_2$ | -0.38 | -3.83 | 0.18 | 0.86 |
| $GaN_2C_2$ | 0.17 | -3.23 | 0.16 | 0.64 |
| $InN_2C_2$ | -0.08 | -3.36 | 0.12 | 0.63 |
| $TlN_2C_2$ | 0.63 | -2.35 | 0.10 | 0.72 |
| $GeN_2C_2$ | -1.26 | -3.56 | 0.15 | 0.65 |
| $SnN_2C_2$ | -0.90 | -3.15 | 0.12 | 0.75 |
| $PbN_2C_2$ | 0.68 | -1.63 | 0.07 | 0.72 |
| $SbN_2C_2$ | -0.56 | -2.01 | 0.09 | 0.74 |
| $BiN_2C_2$ | 0.92 | -1.58 | 0.05 | 0.73 |
| $AlC_4$ | -0.37 | -3.67 | 0.18 | 0.80 |
| $GaC_4$ | 0.24 | -3.08 | 0.16 | 0.70 |
| $InC_4$ | -0.10 | -3.32 | 0.13 | 0.59 |
| $TlC_4$ | 0.67 | -2.46 | 0.11 | 0.76 |
| $GeC_4$ | -0.72 | -3.59 | 0.16 | 0.61 |
| $SnC_4$ | -0.49 | -3.18 | 0.13 | 0.61 |
| $PbC_4$ | 1.42 | -1.59 | 0.06 | 0.80 |
| $SbC_4$ | -0.19 | -2.42 | 0.12 | 0.71 |
| $BiC_4$ | 1.53 | -2.09 | 0.08 | 0.78 |

Table S7. Convergence test for k-point mesh for the adsorption energies of OH* on the $InC_4$.

| K-point | 1×1×1 | 2×2×1 | 3×3×1 | 4×4×1 |
|---|---|---|---|---|
| $E_{ads}$ (eV) | -3.32 | -3.21 | -3.24 | -3.25 |

Table S8. The optimized lattice constants (a×b×c) of PM/N/C SACs embedded graphene sheets (α = β = 90°, γ = 120°). All results are in unit of Å.

| PM moiety | Lattice constants (a×b×c) |
|---|---|
| $AlN_4$ | 12.29 ×12.29 ×20 |
| $GaN_4$ | 12.31 ×12.31 ×20 |
| $InN_4$ | 12.28 ×12.28 ×20 |
| $TlN_4$ | 12.29 ×12.29 ×20 |
| $GeN_4$ | 12.28 ×12.28 ×20 |
| $SnN_4$ | 12.29 ×12.29 ×20 |
| $PbN_4$ | 12.29 ×12.29 ×20 |
| $SbN_4$ | 12.29 ×12.29 ×20 |
| $BiN_4$ | 12.29 ×12.29 ×20 |
| $AlN_2C_2$ | 12.34 ×12.34 ×20 |
| $GaN_2C_2$ | 12.36 ×12.36 ×20 |
| $InN_2C_2$ | 12.34 ×12.34 ×20 |
| $TlN_2C_2$ | 12.31 ×12.31 ×20 |
| $GeN_2C_2$ | 12.34 ×12.34 ×20 |
| $SnN_2C_2$ | 12.32 ×12.32 ×20 |
| $PbN_2C_2$ | 12.31 ×12.31 ×20 |
| $SbN_2C_2$ | 12.32 ×12.32 ×20 |
| $BiN_2C_2$ | 12.31 ×12.31 ×20 |
| $AlC_4$ | 12.39 ×12.39 ×20 |
| $GaC_4$ | 12.38 ×12.38 ×20 |
| $InC_4$ | 12.31 ×12.31 ×20 |
| $TlC_4$ | 12.42 ×12.42 ×20 |
| $GeC_4$ | 12.38 ×12.38 ×20 |
| $SnC_4$ | 12.31 ×12.31 ×20 |
| $PbC_4$ | 12.32 ×12.32 ×20 |
| $SbC_4$ | 12.34 ×12.34 ×20 |
| $BiC_4$ | 12.34 ×12.34 ×20 |

**Reference**


1 B. Delley, From molecules to solids with the DMol$^3$ approach, *J. Chem. Phys.*, 2000, **113**, 7756–7764.

2 D. D. Koelling and B. N. Harmon, A technique for relativistic spin-polarised calculations, *J. Phys. C Solid State Phys.*, 1977, **10**, 3107–3114.

3 C. Zhou, Z. Song, Z. Zhang, H. Yang, B. Wang, J. Yu and L. Sun, DFT studies of elemental mercury oxidation mechanism by gaseous advanced oxidation method: Co-interaction with $H_2O_2$ on $Fe_3O_4$(111) surface, *Appl. Surf. Sci.*, 2017, **426**, 647–655.

4 J. P. Perdew, K. Burke and M. Ernzerhof, Generalized Gradient Approximation Made Simple, *Phys. Rev. Lett.*, 1996, **77**, 3865–3868.

5 B. Hammer and J. K. Nørskov, in *Impact of Surface Science on Catalysis*, Academic Press, 2000, vol. 45, pp. 71–129.

6 Y. Sha, T. H. Yu, Y. Liu, B. V. Merinov and W. A. Goddard, Theoretical Study of Solvent Effects on the Platinum-Catalyzed Oxygen Reduction Reaction, *J. Phys. Chem. Lett.*, 2010, **1**, 856–861.

7 B. Delley, The conductor-like screening model for polymers and surfaces, *Molecular Simulation*, 2006, **32**, 117–123.

8 F. Ortmann, F. Bechstedt and W. G, Schmidt, Semiempirical van Der Waals Correction to the Density Functional Description of Solids and Molecular Structures, *Phys. Rev. B*, 2006, **73**, 205101.

9 K. Chen, Y. Zhang, J. Xiang, X. Zhao, X. Li and K. Chu, p-Block Antimony Single-Atom Catalysts for Nitric Oxide Electroreduction to Ammonia, *ACS Energy Lett.*,

2023, **8**, 1281–1288.

10 Y. Gu, B. J. Xi, H. Zhang, Y. C. Ma and S. L. Xiong, Activation of Main-Group Antimony Atomic Sites for Oxygen Reduction Catalysis, *Angew. Chem. Int. Ed.*, 2022, **61**, e202202200.

11 D. Zhang, L. Gong, J. Ma, X. Wang, L. Zhang and Z. Xia, Disperse Multimetal Atom-Doped Carbon as Efficient Bifunctional Electrocatalysts for Oxygen Reduction and Evolution Reactions: Design Strategies, *J. Phys. Chem. C*, 2020, **124**, 27387–27395.